Title
Structure of iridium oxide catalysts dictates performance differences for proton exchange membrane water electrolyzers

Journal
Journal of Materials Chemistry A, 14(6)

ISSN
2050-7488

Authors
Kwon, Obeen
Shibata, Masao Suzuki
Hamlyn, Rebecca
et al.

Publication Date
2026-01-22

DOI
10.1039/d5ta08192k

Journal of
Materials Chemistry A

Materials for energy and sustainability

Accepted Manuscript

This article can be cited before page numbers have been issued, to do this please use: O. Kwon, M. Suzuki Shibata, R. Hamlyn, J. Oh, J. T. Lang, C. Wang, S. Boettcher, C. Korzeniewski, E. Crumlin, M. J. Zachman, Y. Morimoto and I. V. Zenyuk, *J. Mater. Chem. A*, 2025, DOI: 10.1039/D5TA08192K.

ROYAL SOCIETY OF CHEMISTRY

rsc.li/materials-a

View Article Online
DOI: 10.1039/D5TA08192K

ARTICLE

Structure of Iridium Oxide Catalysts Dictates Performance Differences for Proton Exchange Membrane Water Electrolyzers

Received 00th January 20xx,
Accepted 00th January 20xx

DOI: 10.1039/x0xx00000x

Obeen Kwon[a], Masao Suzuki Shibata[a,c], Rebecca Hamlyn[e], Juhyun Oh[f], Jack T. Lang[a], Cliffton Wang[a], Shannon W. Boettcher[h], Carol Korzeniewski[g], Ethan J. Crumlin[d,e], Michael J. Zachman[f], Yu Morimoto[a*], Iryna V. Zenyuk[a,b*]

Proton exchange membrane water electrolyzers (PEMWEs) are promising zero-emission technologies. However, their high cost remains a barrier to widespread adoption. Iridium oxide is commonly used as an oxygen evolution reaction (OER) catalyst, and its cost and scarcity make it essential to reduce its loading while increasing its activity. Evaluation of iridium oxide activity should be carried out in the membrane electrode assembly (MEA) configuration to replicate realistic operating conditions. Herein, we present a comprehensive benchmarking framework to accurately evaluate the amorphous and crystalline iridium oxides at the MEA level. By systematically varying the catalyst loading, this study confirmed that each MEA was utilized uniformly, presenting intrinsic electrochemical properties independent of the loading. Through intrinsic charge density by voltammetry, we established two electrochemical descriptors that evaluated catalyst redox reactions. The mass activity was evaluated by correlating a current vs. loading, and the slope provides loading-independent mass activity. The effect of the porous transport layer on OER activity was discussed, identifying a 'background' current at zero-loading. This study highlights potential pitfalls in MEA-level catalyst screening and underscores the importance of the loading study for reliable results.

1. Introduction

Energy security for the grid is challenged by solar and wind energy intermittency, requiring short and long-term energy storage solutions[1, 2]. Proton exchange membrane water electrolyzers (PEMWEs) offer a promising energy conversion and storage system, which converts excess grid electricity into green hydrogen, which can, in turn, be used as a fuel in the transportation sector, a chemical for Haber-Bosch process, refineries, and a reducing agent for clean steel manufacturing[1, 3, 4]. Despite noteworthy technological advancements over several decades, the PEMWEs still face many barriers to broad GW-scale deployment needed to meet the US decarbonation targets by 2050[3]. Although PEMWEs have a compact design, can operate at differential pressure, enabling pressurization of hydrogen to 30 bar_g, and do not require management of potassium hydroxide, as liquid alkaline technologies do, PEMWEs are more costly than liquid alkaline electrolyzers[5, 6]. The biggest portion of the overall cost in PEMWEs is attributed to the catalyst, which is based on iridium, one of the scarcest elements, which is utilized for the oxygen evolution reaction (OER) at the anode[7]. Therefore, reducing catalyst loading while improving catalytic activity and stability needs to be accomplished to enable broad deployment of PEMWEs[8].

The iridium oxide catalysts are generally categorized, depending on their atomic structure, into amorphous or crystalline[9, 10]. Iridium oxide catalysts are subjected to the trade-off relationship between catalytic activity and stability given their atomic structure[11, 12]. Amorphous iridium oxide usually shows higher catalytic activity, yet stability is limited compared to crystalline iridium oxide[13-15]. In the amorphous iridium oxide catalyst, the OER likely proceeds through a lattice oxygen reaction mechanism based on coordinatively unsaturated sites with weakened Ir–O bonds, thereby boosting OER activity[16, 17]. Another suggestion in literature is that the reaction takes place not only on the surface of the catalyst but also within its bulk structure[14]. For the crystalline iridium oxide catalyst, the OER mostly follows the adsorbate evolution reaction mechanism through strong Ir–O bonds, producing oxygen from adsorbed water molecules[18]. However, the possibility of lattice oxygen participation has also been

[a] Department of Chemical & Biomolecular Engineering, National Fuel Cell Research Center, University of California, Irvine, Irvine, CA 92697, USA
[b] Department of Materials Science & Engineering, University of California, Irvine, Irvine, CA 92697, USA
[c] Energy Conversion Group, Lawrence Berkeley National Laboratory, 1 Cyclotron Road, Berkeley, CA 94720, USA
[d] Chemical Sciences Division, Lawrence Berkeley National Laboratory, Berkeley, CA, USA
[e] Advanced Light Source, Lawrence Berkeley National Laboratory, Berkeley, CA, USA
[f] Center for Nanophase Materials Sciences, Oak Ridge National Laboratory, Oak Ridge, TN 37831, USA
[g] Department of Chemistry and Biochemistry, Texas Tech University, Lubbock, TX, USA
[h] Department of Chemical & Biomolecular Engineering and Department of Chemistry, University of California, Berkeley, and Energy Storage and Distributed Resources Division, Lawrence Berkeley National Laboratory, Berkeley, CA 94720, USA

Supplementary Information available: [details of any supplementary information available should be included here]. See DOI: 10.1039/x0xx00000x

View Article Online
DOI: 10.1039/D5TA08192K

suggested for crystalline iridium oxide because it also suffers non-negligible dissolution[19-21]. Also, a recent study proposed alternative reaction pathways on crystalline IrO_2 (110) facets, questioning the existing adsorbate evolution reaction mechanism[22]. Therefore, a fundamental understanding of structural differences in iridium oxides is needed to properly evaluate their catalytic activity when integrated as the anode catalyst in PEMWEs.

On the membrane-electrode assembly (MEA) scale, the fundamental understanding of catalytic activity of iridium oxide catalysts is more challenging due to catalyst-ionomer interaction[23, 24], catalyst layer–porous transport layer (PTL) interfacial contact[25] and the local pH variation at the anode[26]. Other factors are thought to cause gaps in measured catalytic activity of iridium oxide using the three-electrode system and the MEA level[27, 28]. Recent studies have attempted to quantify catalytic activity within the MEA for water electrolyzers by varying catalyst loadings for IrO_x[29] to evaluate the Tafel slope or voltammetric charge as a function of the catalyst loading. However, several issues regarding interfacial contact or catalyst utilization were observed, and hence many intrinsic properties of IrO_x showed dependency on the catalyst loading, which should not be the case. Another study compared iridium oxide catalyst structures (amorphous and crystalline) with different iridium packing density or electrical conductivity[30], suggesting the optimal conditions to achieve higher conductivity and higher OER activity. The above MEA studies provided crucial insights into the future design guidelines for optimal catalyst layers. Recently, the degradation mechanism of IrO_x was studied under dynamic operating conditions, quantifying Ir dissolution and transport pathways within the MEA[31]. Similarly, the dissolution of Pt from PTL coating was reported, suggesting the Pt within the membrane likely accelerates the chemical degradation of the membrane[32]. However, the intrinsic catalytic activity of IrO_x catalysts, independent of the catalyst loading, is still difficult to acquire either in MEA or three-electrode systems.

There are important factors on the MEA-level that govern MEA performance and should be systematically accounted for or eliminated to accurately measure OER catalyst activity. The interfacial contact at the catalyst layer|PTL interface should not be overlooked, especially for low-loading catalyst layers, where in-plane electron transport within the catalyst layer can be inhibited. Typical PTLs have larger pore sizes (20–40 µm), as well as higher surface roughness with poor interfacial contact than the carbon gas diffusion layer (GDL) used for fuel cells featuring a fine microporous layer (MPL) with pores of 1 µm of size or so[33]. These morphological properties of the PTL can result in lower catalyst utilization, especially for MEAs with lower catalyst loadings[34, 35]. Another issue that should not be overlooked is using PTL with large pore sizes, unlike sintered PTLs, fiber PTLs have higher pore sizes and porosities[32]. These challenges can be mitigated when the MPL is included with PTLs, thereby securing stable operation[25] with almost identical ohmic loss from interfacial contact for various catalyst loading[36]. However, currently, there are no commercially available PTLs with MPLs, making this mitigation strategy not viable for the majority of the research groups.

While prior MEA studies provide crucial insights on iridium oxides structural differences, there are few works to obtain the intrinsic electrochemical properties by varying catalyst loading. Therefore, this work outlines a comprehensive characterization framework that can be applied as a benchmarking study to any iridium oxide catalysts within the MEA for PEMWE. First, physical characterization with various techniques was conducted to identify the structure and surface properties of the two selected catalysts, amorphous IrOx and crystalline IrO2, from powder to MEA. We conducted a well-designed catalyst loading study to demonstrate this framework; electrochemical characterization is supported by physical characterization to quantify intrinsic catalyst properties on the MEA level. The possible pitfalls and the solutions to various problems encountered are discussed as well. First, we present the redox behavior of the two iridium oxides at different loadings using cyclic voltammetry (CV), reporting the total charge per unit mass (Qm) for each iridium oxide as an intrinsic property. To ensure complete utilization of IrOx catalyst, we replace the PTL with a carbon-based GDL for CV studies to understand the charge contribution of PTL. This consists of two types of charges (capacitive and pseudocapacitive) and compares what contribution is pronounced depending on the iridium oxide structure by showing charge breakdown. We further examine the redox behaviors of iridium oxides using pseudocapacitive charge, establishing two key descriptors to investigate the major differences in their reaction mechanism without advanced physical characterization methods. Next, we report the PEMWE performances and obtain OER activity, which is an intrinsic property independent of catalyst loading. When correlating current as a function of loading, we observed that the current intercept at zero loading is not zero. This zero-loading intercept shows logarithmic behavior with potential, indicating the electrochemical reaction is responsible for such a 'background' current. Our finding highlights the limitations of evaluation for mass activity with a single catalyst loading. Ultimately, our comprehensive framework enables a more accurate evaluation of MEA-level catalyst screening, in addition to a deeper understanding of iridium oxide catalyst properties via advanced physical and electrochemical characterization.

2. Results

2.1 Catalyst structure and morphology analysis

Extensive, *ex-situ* physical characterization was performed to study the crystal structure of each of the catalysts studied, bulk and surface chemical composition, as well, as morphological properties. Fig. 1a shows the different crystallinity between the two iridium oxides by X-ray diffraction (XRD) patterns. The amorphous IrO_x shows a broad peak around 34°, and the pattern of crystalline IrO_2 corresponds to the tetragonal iridium oxide, which are consistent with other typical iridium oxides[37, 38]. Ir metal was not detected through XRD. *Ex-situ* Raman

View Article Online
DOI: 10.1039/D5TA08102K

spectroscopy shows that the B_{2g} vibration of crystalline IrO_2 (719 cm^{-1}) is also resolvable within the envelope of the 743 cm^{-1} peak (A_{1g}) (Fig. 1b)[39]. In contrast, a broad feature near 487 cm^{-1} (labeled as *a*) displaying a shoulder at 604 cm^{-1} (labeled as *b*) is dominant in the spectra of the amorphous IrO_x. A weaker feature near 740 cm^{-1} is also evident (labeled as *c*). The bands in spectra of the amorphous have been traced to Ir–O vibrations[40, 41], some with coupled contributions from –OH moieties.

overlap, and, therefore, the O 1s yields more information for this discernment. The O 1s shows much more of a difference between IrO_x and IrO_2 surfaces, with a significant increase in hydroxide species (M–OH) for the amorphous IrO_x, whereas iridium oxide species is the most pronounced in crystalline IrO_2 (Fig. 1c, Table S2). A previous study has shown that amorphous IrO_x showed higher μ_1–O(H) species, while μ_2–O(H) species were higher for crystalline IrO_2 attributing them to the surface

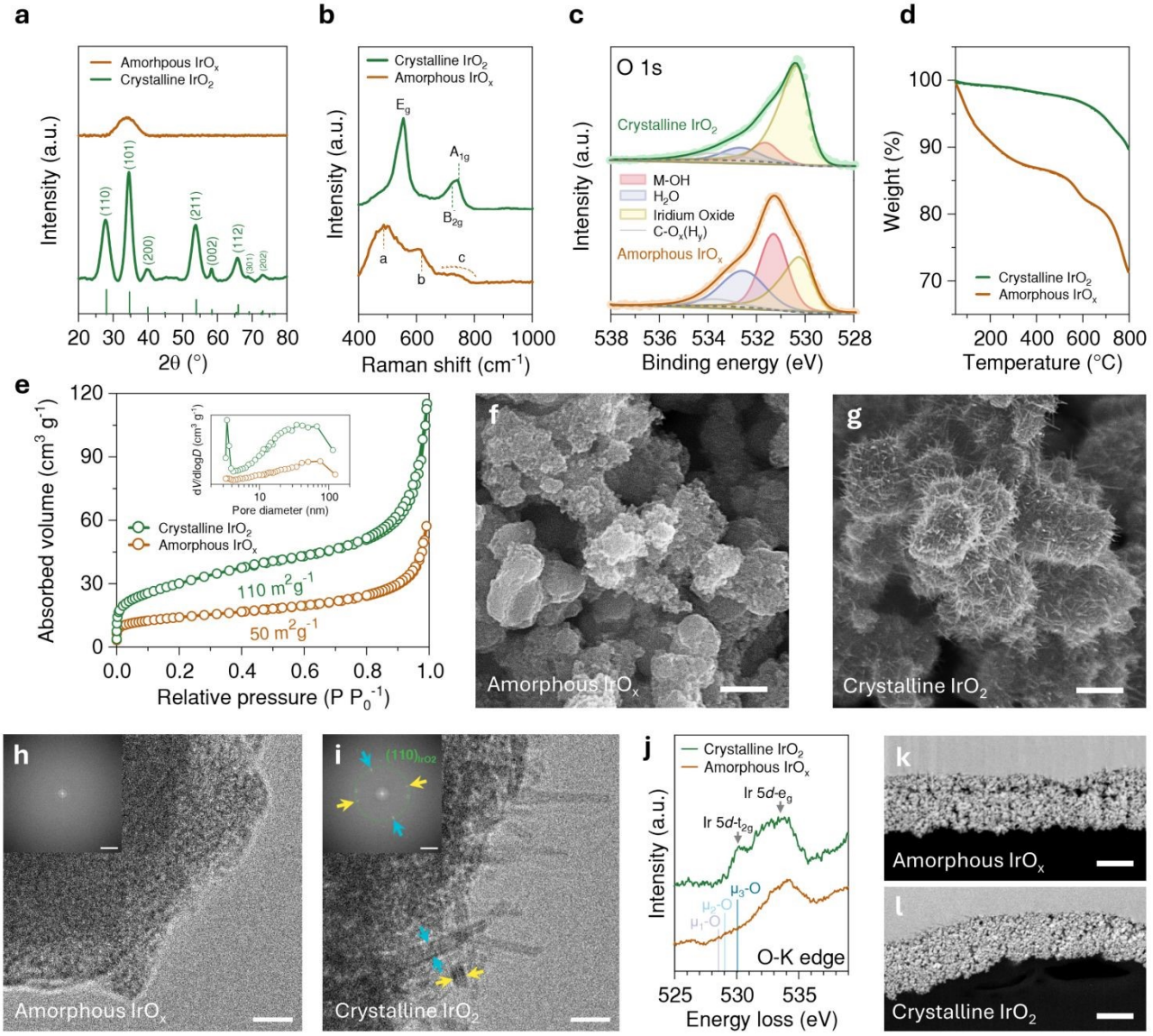

Fig. 1 *Ex-situ* structure and morphology analysis for amorphous IrO_x and crystalline IrO_2. **a**, XRD patterns. **b**, Raman spectroscopy. **c**, O 1s spectra. **d**, TGA curves. **e**, N_2 sorption isotherms (inset) pore size distribution. **f**,**g**, SEM images of (f) amorphous IrO_x and (g) crystalline IrO_2. **h**,**i**, Cryogenic transmission electron microscopy (cryo-TEM) images reveal the nanoscale structure of (h) amorphous IrO_x and (i) crystalline IrO_2, which consist of agglomerated rounded and needle-like structures, respectively. The inset in (i) is the fast Fourier transform (FFT) of this image, showing rutile IrO_2 (110) lattice planes, indicated by colored arrows in the inset and correspondingly in real space. **j**, Average O K-edge electron energy loss spectra, after background subtraction, with edge energies of various possible Ir-O bonds marked[14]. **k**,**l**, pFIB-SEM cross-sectional images of MEAs for (k) amorphous IrO_x and (l) crystalline IrO_2. Scale bars, 100 nm (f,g), 10 nm (h,i), 2 nm^{-1} inset of (h,i), and 1 µm (k,l).

From the XPS measurements, the Ir 4f spectra are nearly identical between the amorphous and crystalline iridium oxides, and so differences are slim (Fig. S1). The 4^+ state is the primary species detected, with some $3/5^+$ and $IrCl_3$ as minor species (Table S1). It is very difficult to separate these species in the Ir 4f spectra, in part due to the highly hybridized nature of these materials and complex peak shapes with significant defects[42], which are identical in their position (eV) to M–OH species with μ_1–O(H) and iridium oxide species with μ_2–O(H).

Thermogravimetric analysis (TGA) shows a drastic weight loss of ~30 % for amorphous IrO_x with increase in temperature up to 800 °C, whereas crystalline IrO_2 lost only ~10 % (Fig. 1d). This might be attributed to the dehydration, desorption of water followed by loss of lattice water with surface defects

(temperature range of 140–400 °C)[38, 43], namely, oxygen-deficient species, which is consistent with O 1s XPS results. The TGA analysis is also consistent with the manufacturer specification, where IrO_x is specified to have 68.38 wt% of Ir, but for IrO_2 the 80.59 wt% of Ir does not match well due to the temperature range of TGA analysis in this study. For crystalline IrO_2, at temperatures above 800 °C the decomposition into metallic Ir happens[43]. This is probably because crystalline IrO_2 contains stable species of μ_3–O, thereby maintaining weight at higher temperatures compared to amorphous IrO_x.

Based on the N_2 isotherm (Fig. 1e), the BET-specific surface area (BET SSA) for crystalline IrO_2 is 110 $m^2 g^{-1}$, which is 2.2 times as higher as that of amorphous IrO_x (50 $m^2 g^{-1}$). Crystalline IrO_2 has a much smaller mean pore size, too. It is highly unusual for crystalline IrO_2 catalyst to have a higher surface area than amorphous, as typically crystalline IrO_2 is obtained through a heat treatment process of IrO_x material during which oxygen loss is observed and particle size increase observed, resulting in a loss of surface area[15]. While the preparation process of this crystalline iridium oxides is not disclosed, the higher surface area and nano-needles confirmed through scanning electron microscopy (SEM) images (Fig. 1f,g) suggest that the preparation process should be different from the typical simple heat treatment. The reproducibility of BET SSA is confirmed in Fig. S4.

High-resolution cryogenic transmission electron microscopy (cryo-TEM) is used to reveal distinct nanoscale structural differences between crystalline IrO_2 and amorphous IrO_x catalysts (Fig. 1h,i and Fig. S2). The amorphous IrO_x catalyst exhibits rounded structures (Fig. 1h, S2a), whereas the crystalline IrO_2 catalyst (Fig. 1i, S2b) consists of agglomerated, needle-like nanostructures, resulting in a spiny surface morphology. Furthermore, (110) lattice fringes in the needle-shaped nanocrystals are oriented perpendicularly to the long axis of the structures, as highlighted in the inset of Fig. 1(i), which is consistent with previous observations of IrO_2 nanorods[44].

To gain deeper insights into the physical and electronic structure of these catalysts, we performed cryogenic scanning transmission electron microscopy with electron energy loss spectroscopy (cryo-STEM EELS) (Fig. 1j). The oxygen K-edge spectrum of the crystalline IrO_2 displays two distinct peaks at 530 eV and 534 eV that correspond to O 2*p*–Ir 5*d* hybridized states. These are due to a local octahedral bonding environment around the Ir atoms that results in a crystal field splitting of the Ir 5*d* states into Ir 5*d*-t_{2g} and Ir 5*d*-e_g states, consistent with a rutile structure[45]. In contrast, these sharp peaks were absent for amorphous IrO_x, replaced by a gradual slope that suggests a lack of a uniform crystal bonding environment in the amorphous phase, which likely contains a variety of Ir–O bonds. These findings are consistent with recent *operando* X-ray absorption spectroscopy (XAS)[14], which similarly reported a diminished 530 eV 'IrO_2' peak for amorphous IrO_x and attributed remaining features in this energy range to oxygen atoms with one, two, or three bonds to neighboring iridium atoms, which they designated μ_1–O, μ_2–O, and μ_3–O, respectively. While a gradual slope is present in this range rather than specific, distinct peaks, it suggests species such as these may contribute to amorphous IrO_x catalyst spectra.

Further elemental analysis via STEM energy-dispersive X-ray spectroscopy (EDS) reveals that the oxygen of both catalysts was uniformly distributed on the scale of hundreds of nm (Fig. S3), with amorphous IrO_x having an average oxygen content ~1.5 times as high as that of crystalline IrO_2. This, combined with our EELS results, suggests that excess oxygen that is not fully bonded to iridium is present in the amorphous catalyst and indicates the presence of water, as shown by the above XPS results and TGA analysis.

We prepared eight MEAs to investigate the PEMWE performance as well as intrinsic catalytic activity depending on catalyst structure and iridium oxide loading at the anode (0.10, 0.26, 0.35, and 0.85 $mg_{IrOx\ or\ IrO2}$ cm^{-2} for each iridium oxide structure). The single-cell configuration is the same except for the anode catalyst loading and iridium oxide structure (see Methods). Fig. 1k,l illustrates the cross-sectional images of the anode catalyst layer of 0.85 mg cm^{-2} loading, demonstrating comparable thicknesses of 1.69 ± 0.21 µm (amorphous IrO_x) and 1.58 ± 0.18 µm (crystalline IrO_2). Furthermore, we confirm the uniformity of both catalyst layers through 3D visualization shown through the reconstruction of ~180 μm^2 (amorphous IrO_x) and ~442 μm^2 (crystalline IrO_2), as shown in Fig. S5.

The sheet resistance is plotted against the loading and the inverse of the loading in Fig. S6a and b, respectively. Clearly, the catalyst layer with amorphous IrO_x showed higher sheet resistances than the crystalline with the same loading. Although the linear relations are seen with the loading for both the catalysts in Fig. S6b, the extrapolation to zero (infinite loading) is not close to zero resistance. This suggests that at the higher the loading the connectivity is worse. A possible cause can be a crack formation during the catalyst layer drying, which can be more likely for thicker layers. The surface morphology of the anode iridium oxide decal is presented in Fig. S7, which was used to become an anode catalyst layer. Namely, this shows the interface directly facing the membrane. Even for the highest loading for both decals (0.85 mg cm^{-2}), we observe the micrometer scale voids. However, it is uncertain how those voids contribute to the in-plane electron resistance. Moreover, it is also uncertain how those sheet resistances affect the electrochemical properties of the MEAs because the effect of the sheet resistance should be discussed considering the pore opening size of the MPL attached to the catalyst layer[30, 46].

2.2 Study of catalyst utilization using PTL and carbon-based GDL

Cyclic voltammetry (CV) was performed for the amorphous and crystalline iridium oxides MEAs having different anode catalyst loading (Fig. S8,9). The amorphous IrO_x shows two pronounced redox peaks at around 0.8 and 1.2 V. Crystalline IrO_2 shows one broad peak between 0.5 and 1.2 V, which has been previously reported[19]. Furthermore, the shapes of CVs for both of the iridium oxides show a symmetry between anodic and cathodic scans, indicating that the redox reactions are highly reversible.

Pt-coated PTL was used in these studies, where Pt is electrochemically active and can contribute to pseudo double

View Article Online
DOI: 10.1039/D5TA08192K

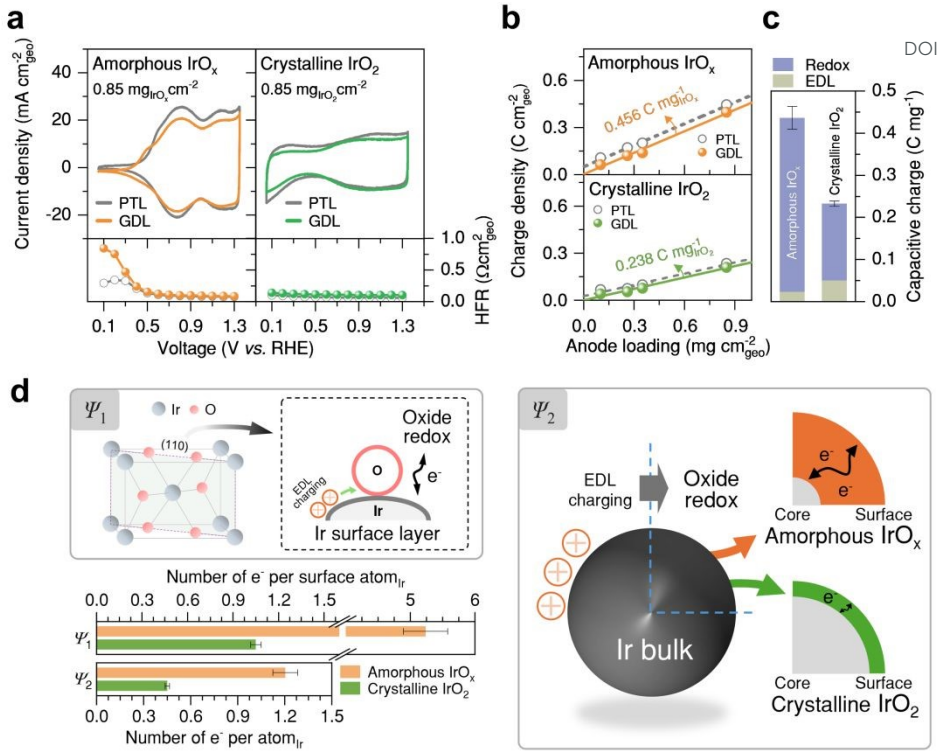

Fig. 2 CV analysis for amorphous IrO_x and crystalline IrO_2. a, CV and HFR recorded with 50 mV s^{-1} for MEAs in the configuration of PTL and GDL at the anode with iridium oxide loading (0.85 mg cm^{-2}) with a range from 0.05 to 1.35 V RHE. **b**, Total charge per unit iridium oxide mass (Q_m) in amorphous IrO_x and crystalline IrO_2 obtained from linear correlation in geometric charge density (Q_{geo}) at 50 mV s^{-1} against the anode loading (0.10, 0.26, 0.35, and 0.85 mg cm^{-2} for both iridium oxide catalysts). The MEAs with PTL or GDL configurations at the anode were compared to clarify the effect of PTL, which is shown by the y-intercepts of this plot. **c**, Q_m breakdown of iridium oxide with different structures, which consists of an EDL and redox. EDL charge is calculated via BET surface areas and the specific capacitance of metal oxide catalysts under acidic media (0.035 mF cm^{-2}_{oxide})[47]. The redox charges were obtained by the difference between the total charge and EDL charge. **d**, The number of electrons in the redox reaction during the given range of CV; Ψ_1 for the number of electrons per surface iridium atom, and Ψ_2 for the number of electrons per iridium atom. All error bars were standard deviations obtained from the calculation of Q_m, Ψ_1, and Ψ_2 in different CV scan rates (25, 50, 100, 125, 150, and 200 mV s^{-1}).

layer capacitance. To understand Pt contribution to the measured CVs, MEA was built without IrO_x catalyst layer and only Pt-coated PTL was in contact with membrane. Fig. S10a shows the CVs of the Pt-coated PTL-only MEA, where Pt fingerprints are clearly observed, and the current density was up to 5 mA cm^{-2} under a scan rate of 200 mV s^{-1}. Furthermore, the Pt-coated PTL-only MEA shows non-negligible OER activity from polarization curves (Fig. S10b), while the MEA with GDL (no Pt coating) shows very small current densities in the polarization curve, mainly from carbon oxidation.

Fig. 2a compares the CV and high-frequency resistance (HFR) results for both iridium oxide catalysts using different diffusion media: Pt-coated Ti PTL (Denora) and carbon GDL (H23C6; Fredenburg), both have a microporous layer. While the PTL is hydrophilic and the MPL has micrometer-scale pores facing the catalyst layer, the GDL is hydrophobic, and the MPLs have pore sizes in the range of tens of nanometers. The CVs in Fig. 2a and Fig. S11 clearly show higher redox currents for the PTL than for the GDL because of the redox and electrochemical double layer (EDL) charge/discharge due to Pt. In addition, Fig. 2a shows an increase in HFR for the amorphous IrO_x below 0.5V for both diffusion layers. This HFR increase indicates conductivity loss of the amorphous IrOx as it transitions at these lower potentials to lower oxidation state. However, the degree of the HFR increase with decrease in potential is less pronounced for the MEA with PTL compared to the GDL. This is likely because the complete reduction of the amorphous IrO_x to a less conductive state is prevented because of the longer in-plane electron conduction due to the larger pore opening of the microporous layer in the PTL.

The current density in the CV was integrated for the whole potential range (0.05–1.35V) to obtain the total charge. The obtained charge density (Q_{geo}) shows good linearity with iridium oxide loading as shown in Fig. 2b. Their slopes give the total charges per unit mass of the iridium oxide (Q_m) and agreed for the GDL and PTL, and the y-intersects give the contributions from each diffusion media, namely, the EDL charge/discharge and the redox reactions of platinum for PTL and negligible contributions for the GDL. The linearity of charge density with the loading indicates that the catalyst is fully utilized at both low and high loadings. The CV analysis across catalyst layer loadings is a critical step in obtaining intrinsic activities for the IrO_x catalyst layers. If non-linearity is observed for the integrated charge density with the loadings, then catalyst disconnection or other utilization issues exist, hindering catalyst activity study.

2.3 Charge breakdown

The total charge (Q_m) consists of the pure capacitive charge from the EDL and the pseudocapacitive charge from the redox reactions of iridium oxide. The former can be roughly estimated from the BET surface area of the catalysts in the catalyst layer and the typical specific capacitance value for oxides, 0.035 mF

cm^{-2}. Fig. 2c (grey bar) shows the EDL portion of the total charge, where higher EDL charge is observed for crystalline iridium oxide because its larger BET. The latter, the redox reaction charges of iridium oxides, can be obtained by subtracting the EDL charge from the total charge, as shown in Fig. 2c (purple bar). Amorphous IrO_x shows both larger total charge and larger redox reactions charge compared to crystalline IrO_2. All error bars in here indicate the standard deviation at different scan rates (25, 50, 75, 100, 150, and 200 mV s^{-1}) to confirm the kinetic-controlled voltametric response.

2.4 Redox reaction analysis

The obtained reaction charges from the CV are due to the redox reactions of iridium oxides and therefore should be able to be further analyzed by calculating the number of reacted electrons per iridium atom. Firstly, the number of iridium atoms on the surface of crystalline iridium oxide was estimated by assuming the rutile iridium oxide structure and the (110) facet, which has the highest planar density. The number of surface iridium atoms of the amorphous IrO_x is hard to estimate, and therefore, the same value as the crystalline was used for the estimation. The details for calculations are found in *Methods*.

The obtained numbers of electrons for the redox reactions per surface iridium atom, denoted by Ψ_1, for crystalline and amorphous iridium oxides are shown in Fig. 2d (first bar graph). For crystalline IrO_2, the Ψ_1 of 1.06 implies that the oxidation state of the surface iridium varies from Ir^{3+} to Ir^{4+}, consistent with the reported literature[48]. The higher Ψ_1 (5.23 of electrons) in amorphous IrO_x indicates that more electrons participate in the redox reactions than in crystalline IrO_2. Even assuming the oxidation state change from Ir^{3+} to Ir^{5+}as reported before[40, 49], the number of electrons of 5.23 is too high to consider that the redox reaction is limited to the surface, indicating the participation of subsurface Ir atoms.

To estimate the degree of subsurface atom participation, the number of reacted electrons per iridium atom in the whole catalyst particles was calculated using the catalyst loadings and iridium metal weight ratio given by the manufacturer (and confirmed through the TGA). The results, as denoted as Ψ_2, are shown in Fig. 2d (second bar graph). The value of Ψ_2 in amorphous IrO_x (1.20) shows that redox reaction in amorphous IrO_x utilizes all iridium atoms if one-electron redox reaction is assumed or about half of them if two-electron redox reaction is assumed. In either case, the subsurface redox reactions cannot utilize only Ir atoms but oxygen lattice will participate too. The bulk IrO_x participation in the reaction can be explained through the OER proceeding through the lattice oxygen mechanism[16, 19, 21] or the presence of specific electron-deficient oxygen species from XPS results[14, 50]. We note that these results are based on various assumptions and rough estimations. Nonetheless, this analysis provides a useful mechanistic insight into the surface vs. bulk participation of the amorphous and crystalline iridium oxides in the OER on the MEA level.

2.5 PEMWE performance depending on anode catalyst loading

In this section, the comparison of PEMWE performance is presented for two catalysts at different loadings, where polarization curves and EIS data are collected to quantify polarization behavior. Fig. 3a compares the PEMWE performance of the MEAs at 60 °C for 0.10, 0.26, 0.35, and 0.85 mg cm^{-2} loadings. The highest anode loading of 0.85 mg cm^{-2} shows the best performance for the entire current density range for each of the catalysts. Furthermore, at each loading, the amorphous IrO_x catalyst layers showed better performance than crystalline IrO_2 (Fig. S12). Fig. S13 summarizes the PEMWE performance of all MEAs at given potentials (1.8 and 2.0 V) by comparing their current density. The MEAs of amorphous iridium oxide exhibit an overall higher performance than those of the crystalline one. The highest current density at 2.0 V is confirmed at 6.2 A cm^{-2} (0.85 mg cm^{-2} of amorphous IrO_x) and 5.9 A cm^{-2} (0.85 mg cm^{-2} crystalline IrO_2), respectively. Specifically, the amorphous IrO_x of 0.10 mg cm^{-2} shows 2.9 A cm^{-2} at 1.8 V, comparable to the 2026 US Department of Energy (DOE) technical targets.

The lower anode loading shows a slightly higher HFR on the entire current density range for both iridium oxide catalysts (e.g., HFR at 1.5 V is shown in Table S3), probably having electron transport resistance due to poor interfacial contact between the anode catalyst layer and PTL[51] or higher sheet resistance (Fig. S6a). Fig. S14a,b compares the EIS results of MEAs with different anode iridium oxide loadings for amorphous or crystalline catalysts. Three potentials were selected for EIS analysis: 1.s5 V (kinetic region), 1.8 V (ohmic region), and 2.0 V (high current density region) to better understand resistances across the entire PEMWE polarization range. The HFR of all MEAs shows small differences among them (up to <8 mΩ cm^2). From the sheet resistance measurement results (Fig. S6) and thickness estimation by FIB-SEM image (Fig. 1k,l), the through-plane electronic resistance was roughly estimated assuming isotropy as ~0.1 mΩ cm^2 for 0.85 mg cm^{-2} of amorphous IrO_x as the highest resistance case. Therefore, the electronic resistance within the catalyst layer can be safely regarded as negligible. The charge transfer (R_{ct}) resistance and catalytic activity are discussed in the next section using HFR-corrected polarization curves.

2.6 OER activity

HFR-corrected polarization curves are plotted in Fig. 3a, and Tafel plots are plotted in Fig. 3b, respectively. The Tafel slope shows clearly straight lines for all the loadings and catalysts. This indicates that all the HFR-corrected polarization curves are controlled by the OER kinetics in the low current density regime. The difference between the Tafel slope of the crystalline and that of amorphous suggests a difference in the reaction mechanisms, but the discussion on the details of the reaction mechanisms is out of the scope of this paper.

View Article Online
DOI: 10.1039/D5TA08192K

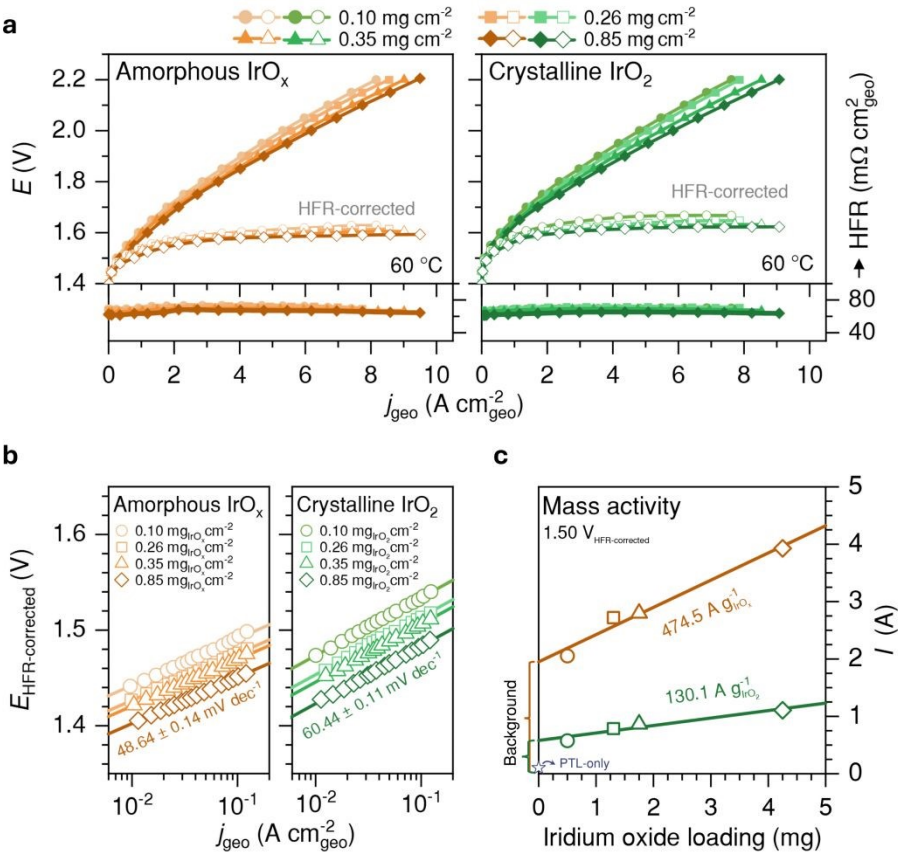

Fig. 3 Evaluation of PEMWE performance from different iridium oxide loading. a, Polarization curves with HFR-corrected curves and HFR in amorphous IrO_x (left) and crystalline IrO_2 (right). PEMWE testing was performed at 60 °C without backpressure and distilled water at the anode. **b**, Tafel slope of different anode loading in amorphous IrO_x (left) and crystalline IrO_2 (right) **c.** OER current density at 1.50 $V_{HFR\text{-}corrected}$, as a function of catalyst loading. The slopes indicate the mass activity (MA) of the iridium oxides, and the y-axis intercepts are the contribution from Pt-coated PTL, as denoted as 'background' and 'PTL-only' for the hollow star symbol.

The OER currents at 1.5 V (HFR-corrected) were plotted as a function of loading in Fig. 3c. A clear straight line was obtained for each catalyst. The slopes of the straight line are the mass activity (MA) of the iridium oxides. However, the y-intersects of the extrapolated straight lines are far above the origin. The current due to Pt-coated PTL only at zero loading (in the MEA when no IrO_x catalyst layer was present) is shown too, which is significantly lower compared to the zero-loadings extrapolated currents in this plot. The effect of Pt-coated PTL is discussed in the next section. The amorphous IrO_x exhibited MA of 474.5 A g_{IrOx}^{-1}, ~3.1 times as high as crystalline IrO_2 of 130.1 A g_{IrO2}^{-1}. These values are within the range of the values reported elsewhere using the MEA or three-electrode system (Table S4). BET specific activity and more analysis on whether only OER kinetics control the polarization behavior across the catalyst loading are discussed in Supplementary Note 1. It is important to note that an equivalent of Tafel slope increase in voltage is expected in the kinetic regime when the IrO_x loadings decrease by one magnitude[52].

2.7 Understanding of the extrapolated or 'background' current at zero iridium oxide loading

It is important to note that the MA was obtained by the slope of the OER current as a function of catalyst loading. However, MA has been typically reported as the measured geometric current density divided by catalyst loading at a single point[19, 53, 54]. This approach presumes that the current density must be zero for the catalyst loading of zero. However, the MEA testing is more complex than the typical three-electrode setup[27]. Earlier, we saw the background effect from the Pt-coated PTL on the capacitive charge from the CV. Here again, we observed non-zero y intersects in the OER current vs. loading plot, which cannot be explained without considering the effect of Pt-coated PTL.

To clarify the nature and behavior of the background effect, the background current was collected from the HFR-corrected potentials ranging from 1.40 to 1.55 V and extracted from the plot of the linear relationship between the geometric current density and anode loading (Fig. S15), which is plotted in Fig. 4. This shows a clear Tafel-like current-potential relation and carries the same slope for both catalysts layers but different values. This Tefel-like background shows that this effect is not due to either experimental errors like short-circuit or correlation errors (Table S6) but due to actual electrochemical phenomena. The difference in the current density values between the amorphous and crystalline iridium oxides suggests that these background currents are not simple OER currents on Pt-coated PTL itself but that some interaction between the Pt from the PTL and iridium oxides may play an important role. This observation is supported by recent findings of Pt dissolution

View Article Online
DOI: 10.1039/D5TA08102H

from the PTL while operating PEMWE, thereby confirming the potential electrochemical contribution[32]. It is not clear at this point the exact mechanism of the electrochemical reaction that creates these currents but we are confident to report their presence for all of the MEAs. For this reason, reporting MA based on the single loading of a catalyst should not be a valid practice in our community, and instead, a carefully designed loading study should be carried out to report the true mass activity of a catalyst.

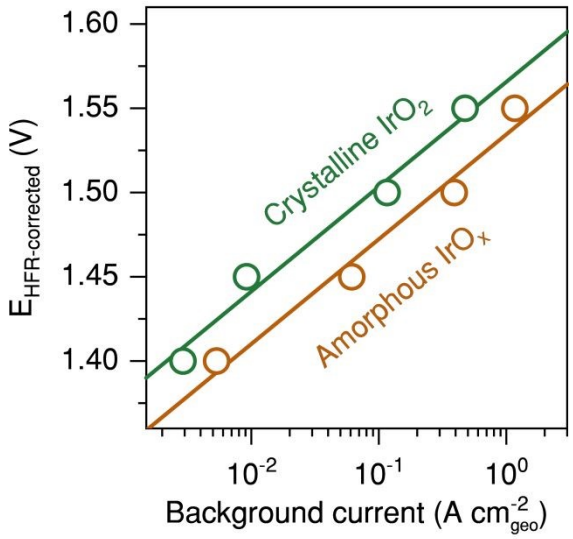

Fig. 4 Background effect on current in iridium oxide with different structures. Background current as a function with log scale of various HFR-corrected potentials of amorphous IrO_x and crystalline IrO_2. Intrinsic activity normalized by anode loading through linear correlation in Fig. 3b or Fig. S15, the non-zero intercept at the loading of zero indicates the background current. The linear correlation from each data point implies the Tafel relation in the background current.

3. Conclusion

We studied the MEAs with four catalyst loadings and two catalysts: amorphous and crystalline iridium oxides. The crystalline IrO_2 exhibits a higher BET SSA than amorphous iridium oxide because of its specific morphology consisting of nano-needles grown on particles. Surface analysis using XPS revealed that the pronounced oxygen-deficient species differed depending on the IrO_x structure, where amorphous IrO_x contained more electrophilic species compared to crystalline. XRD and Raman analysis confirmed the amorphous and crystalline structures of these two catalysts. TEM analysis revealed the nano-needles present on the surface of IrO_2 catalysts and FIB-SEM analysis showed that catalyst layers with the highest loadings (0.85 mg cm^{-2}) showed homogeneous thickness and catalyst distribution.

Total charge analysis from the CV for different catalyst loadings reveals a higher specific charge for amorphous compared to crystalline catalysts. We calculated two descriptors, Ψ_1 and Ψ_2, for two catalysts. Ψ_1 described the number of electrons participating in redox reactions divided by the number of surface atoms, where amorphous IrO_x showed 4.9 times as high as crystalline IrO_2. Ψ_2 is calculated by the number of electrons that participate in redox reactions divided by the total number of Ir atoms in each catalyst, showing about 2.7 times as high as amorphous IrO_x. The PEMWE performance after HFR correction was controlled by OER kinetics regardless of the catalyst loading for each loading. We examined the dependency of OER current on the loading and found that platinum-coated PTL has a certain contribution to the OER. Hence, the precise catalytic activity of the catalyst in the MEA can only be obtained after subtracting the PTL contribution.

The amorphous IrO_x exhibited higher mass activity than the crystalline IrO_2 despite its lower BET SSA. Different Tafel slope of the two catalysts suggests different reaction mechanisms. Although further studies are required to reveal the details of this difference, the subsurface atom participation in the redox reactions of the amorphous suggests that the subsurface atoms also participate in the OER and contribute to its higher activity. We also discovered non-zero 'background' current when current is projected to y-axis at zero loading that cannot be purely explained by Pt contribution from the PTL. The background current showed logarithmic dependence on potential and had different values for IrO_x or IrO_2. If Pt from the PTL was the only contributing factor to this non-zero catalyst loading current, then the current should be the same for both catalysts, but it was not the same. Lastly, we believe that the proposed methodology can be applied to evaluate any OER electrocatalysts and provide valuable insight into the OER and hints for realizing ultra-low iridium oxide loading MEAs, contributing to cost-effective PEMWE technology for green hydrogen production.

4. Methods

4.1 Preparation of MEA

All CCMs were fabricated using the decal transfer method with doctor blade coating. The holistic process of CCM preparation is shown in Fig. S16.

The two types of iridium oxide catalyst powder in this study were provided by Ishifuku Metal Industry. The anode catalyst ink contained powder of amorphous IrO_x (Ir: 68.38 wt%) or crystalline IrO_2 (Ir: 80.59 wt%), ionomer (Nafion POWDion soluble, Ion Power; equivalent weight = 1100), water, and 1-propanol. The ionomer to iridium oxide catalyst (I/C) ratio was 0.15 for all samples, and the weight ratio of contents was calculated as follows: iridium oxide catalyst:ionomer:water:1-propanol = 1:0.15:1.5:3. The anode catalyst ink was sonicated in an ice bath for 1 hr. The dispersed catalyst ink was put onto a 100 μm thick fluorinated ethylene propylene substrate. The micrometer adjustable film applicator (MTI) was utilized to perform doctor blade coating. The ink volume, coating speed, and gap height between the film applicator and substrate were adjusted to prepare different anode catalyst loading (0.10, 0.26, 0.35, and 0.85 $mg_{IrO_x \text{ or } IrO_2}$ cm^{-2}). After coating, as-received decals were dried in a vacuum desiccator for 12 hrs to remove any solvents. The catalyst loading of the anode decal was measured using the Explorer scale (OHAUS) with 0.02 mg cm^{-2}

View Article Online
DOI: 10.1039/D5TA08190K

accuracy. For the cathode side, the pre-made decal (3M) consisted of Pt/C and Nafion ionomer with a catalyst loading of ~0.37 mg_{Pt} cm^{-2}. Prepared anode and cathode decals were carefully transferred to Nafion 212 membrane (Ion Power) using the manual hydraulic press (Specac) by applying 1 ton and a temperature of 130 °C for 10 mins. During the decal transfer, the PTFE sub-gasket was placed on each side of a membrane to secure a 5 cm^2 active area for the catalyst layer. Plus, the membrane was surrounded by a Kapton gasket to prevent compression of the membrane. For the diffusion media, the platinum-coated (100 nm thick) sintered Ti porous transport layer with a microporous layer (DeNora; total thickness of ~320 µm and ~45 µm for microporous layer) for the anode and carbon gas diffusion layer (GDL) of H23C6 (Freudenberg; ~250 µm thick) for the cathode were placed with the CCM for a single cell. Fabric cloth PTFE gaskets were inserted for both diffusion media for optimal compression. The cathode compression was ~20% with using a ~200 µm gasket. Bipolar plates were graphite made with triple serpentine for the cathode and titanium made with parallel for the anode.

4.2 PEMWE testing

Following the single-cell assembly, PEMWE was operated at the homemade water electrolyzer test station under a cell temperature of 60 °C without backpressure (Fig. S17). The distilled water was held to a resistivity of 18.2 MΩ cm using a polymer resin filter. The water was supplied through a peristaltic pump into the anode with 10 sccm under 60 °C. To maintain the reference electrode of PEMWEs, the high purity H_2 gas was supplied at the cathode with 10 sccm.

All electrochemical characterizations in this study were measured using HCP-803 potentiostat (BioLogic). All MEAs were first subjected to a break-in procedure. The voltage was held from 0.8 to 1.2 V (step size of 0.1 V) for 5 mins, and then CV with a scan rate of 2,000 mV s^{-1} was performed for 50 cycles (0.05–1.35 V). Next, the constant current at 0.2 A cm^{-2} was held for 2 hrs. Finally, 100 cycles of CV with a scan rate of 200 mV s^{-1} were conducted from 0.05 V to 1.35 V. After break-in the MEA, CV with scan rates of 25, 50, 75, 100, 150, and 200 mV s^{-1} was measured between 0.05 V and 1.35 V. The HFR for MEAs was measured at the same voltage window for CV. To acquire Tafel slope, the multi-step chronopotentiometry was carried from 4 mA cm^{-2} to 0.4 A cm^{-2} with 25 steps for 45 s hold each. Given the current density range for the Tafel slope is mostly aligned with the Tafel region, confirming a linear relationship with the potential vs. log scale current density. Polarization curves were measured through the multi-step chronoamperometry from 1.35 V to 2.20 V with a step size of 0.05 V for 45 s hold each to ensure stabilization. Right after obtaining polarization curves, the HFR of MEAs was measured by scanning the frequency range from 6 kHz to 1 kHz at a constant potential from 1.35 V to 2.20 V with a step size of 50 mV. Next, electrochemical impedance spectroscopy (EIS) measurements were performed with the frequency range from 100 kHz to 0.1 Hz at a constant potential of 1.5, 1.8, and 2.0 V, respectively.

After PTL was replaced with GDL at the anode, all MEAs were reconditioned to the aforementioned protocols except for constant current hold and Tafel slope acquisition. Namely, only CV and HFR were measured for MEAs with GDL at the anode. There was no change in CV protocol, but EIS was only performed at 1.0 V with the same frequency range to prevent carbon corrosion.

The MEA without an anode catalyst layer (i.e., only PTL or GDL directly contacted the membrane) was tested for CV and polarization curve measurements only. Either cell configurations or testing protocols for CV and polarization curves were the same as mentioned above, except for the MEA without the anode catalyst layer.

4.3 Charge breakdown and redox reaction analysis

The two descriptors (Ψ_1 and Ψ_2) were introduced to investigate redox behavior on amorphous and crystalline iridium oxide. These descriptors were derived using redox charge ($Q_{m/redox}$), an intrinsic electrochemical property for amorphous or crystalline iridium oxide catalysts. The Q_m is the total charge per iridium oxide mass, including EDL and redox reactions. First, the geometric charge density (Q_{geo}) can be calculated by the following equation:

$$Q_{\mathrm{geo}}\ [\mathrm{C\ cm_{geo}^{-2}}] = \frac{\int_{V_1}^{V_2} j\ \mathrm{d}V}{2v} \qquad (1)$$

where v is scan rates from CV, and V_1 and V_2 are lower/upper potential limits of 0.05 V/1.35 V. To consider the half redox reaction, the total geometric charge density was divided by two. The calculated Q_{geo} for each MEA was plotted with respect to the anode loading, and the slope from linear fit indicates Q_m [C mg_{IrOx}^{-1}], which contains charge of capacitive and pseudocapacitive. Next, to exclude the capacitive charge, we assumed that both iridium oxide catalysts follow the specific capacitance of 0.035 mF cm_{ox}^{-2}, which is generally adapted for metal oxide OER catalysts under acidic media[47]. $Q_{m/redox}$ was calculated by excluding capacitive charge, that the specific capacitance was normalized by its BET SSA as follows:

$$Q_{\mathrm{m/redox}}\left[\mathrm{C\ mg_{IrOx}^{-1}}\right] = Q_{\mathrm{m}} - 0.035 \times (V_2 - V_1) \times \mathrm{BET\ SSA} \qquad (2)$$

The descriptors were under the following assumptions: all iridium oxide catalysts are tetragonal IrO_2, showing the highest planar density (PD) at IrO_2(110), considering the number of Ir atoms only. The atomic weight of Ir was 192 g mol^{-1} for both catalysts. These descriptors were calculated for various scan rates (25, 50, 75, 100, 150, and 200 mV s^{-1}), then the standard deviation was obtained for each iridium oxide catalyst.

For Ψ_1, $Q_{m/redox}$ was normalized by BET SSA for given catalysts to get the SSA_{BET}-normalized charge density (Q_{SSA}), shown in Eq. (3). To acquire a charge per unit Ir atom (Q_{atom}), Q_{SSA} was normalized by PD (9.86×10^{14} $atom_{Ir}$ cm^{-2}). Finally, Q_{atom} was divided by elementary charge (1.602×10^{-19} C) to obtain Ψ_1, the number of electrons on the surface of the unit atom for a half redox reaction. The Ψ_1 can be described by the following equations:

$$Q_{\mathrm{SSA}} = \frac{Q_{\mathrm{m/redox}}}{\mathrm{SSA_{BET}}} \qquad (3)$$

$$Q_{\text{atom}} = \frac{Q_{\text{SSA}}}{\text{PD}} \quad (4)$$

$$\Psi_1 = \frac{Q_{\text{atom}}}{1.602\times10^{-19}} \quad (5)$$

For Ψ_2, the Q_m was divided by the Ir weight ratio of given catalysts and elementary charge to obtain the number of electrons per unit Ir mass. Besides that, the number of Ir atoms per unit Ir mass was acquired by which Avogadro's number (N_A) was divided by the Ir atomic weight (192 g mol^{-1}). Therefore, the ratio between the number of electrons per unit Ir mass and the number of Ir atoms per unit Ir mass indicates the number of electrons per Ir atom (Ψ_2) for half redox reaction from Eq. (6).

$$\Psi_2 = \frac{Q_{\text{m/redox}}}{(1.602\times10^{-19})\ (\text{Weight ratio})} \times \frac{192}{N_A} \quad (6)$$

Author contributions

O.K. fabricated MEAs, performed all electrochemical characterizations and physical characterizations of N_2 sorption isotherm, TGA, SEM, and wrote the original draft. C. W. conducted XPS and assisted in data processing. M. S. conceived the EIS model and evaluated EIS fitting. R. H. and E. C. performed XPS analysis and fitting. J. O. and M. J. Z. performed (S)TEM, EELS, and EDS experiments and analyses. C. K. performed Raman spectroscopy measurements and analysis. J. L. and S. B. conducted pFIB-SEM and image analysis. I. Z. and Y. M. supervised this project. I. Z., Y. M., and O.K. conceived the concept of this paper. M .S., R. H., J. O., C. K., and J. L. contributed to writing this paper. All the authors contributed to the proofreading of this manuscript.

Conflicts of interest

The authors declare that they have no known competing financial interests or personal relationships that could have appeared to influence the work reported in this paper.

Data availability

The data supporting this article have been included as part of the ESI.

Acknowledgements

The (S)TEM, EELS, and EDS portions of this research were supported by the Center for Nanophase Materials Sciences (CNMS), which is a US Department of Energy, Office of Science User Facility at Oak Ridge National Laboratory. The authors acknowledge funding from DOE Energy Earthshot Initiative as part of the Center for Ionomer-Based Water Electrolysis, award DE-AC02-05CH11231. We thank Dr. Valerie Brogden for carrying out FIB-SEM measurements at University of Oregon. The authors acknowledge the use of facilities and instrumentation at the University of California, Irvine (UC, Irvine) Materials Research Institute (IMRI), which is supported in part by the National Science Foundation through the UC Irvine Materials Research Science and Engineering Center (DMR-2011967). XPS work was performed using instrumentation funded in part by the National Science Foundation Major Research Instrumentation Program under Grant CHE-1338173. Ishifuku Metal Industry Co. is acknowledged for providing two types of Ishifuku catalyst materials.

View Article Online DOI: 10.1039/D5TA08129K

References

1. E. T. Vogt and B. M. Weckhuysen, *Nature*, 2024, **629**, 295-306.
2. M. Khalid, *Energy Strategy Reviews*, 2024, **51**, 101299.
3. S. G. Nnabuife, E. Oko, B. Kuang, A. Bello, A. P. Onwualu, S. Oyagha and J. Whidborne, *Sustainable Chemistry for Climate Action*, 2023, **2**, 100024.
4. R.-T. Liu, Z.-L. Xu, F.-M. Li, F.-Y. Chen, J.-Y. Yu, Y. Yan, Y. Chen and B. Y. Xia, *Chemical Society Reviews*, 2023.
5. Q. Xu, L. Zhang, J. Zhang, J. Wang, Y. Hu, H. Jiang and C. Li, *EnergyChem*, 2022/09/01, **4**.
6. J. R. Varcoe, P. Atanassov, D. R. Dekel, A. M. Herring, M. A. Hickner, P. A. Kohl, A. R. Kucernak, W. E. Mustain, K. Nijmeijer and K. Scott, *Energy & environmental science*, 2014, **7**, 3135-3191.
7. H. Wu, Y. Wang, Z. Shi, X. Wang, J. Yang, M. Xiao, J. Ge, W. Xing and C. Liu, *Journal of Materials Chemistry A*, 2022, **10**, 13170-13189.
8. J. Murawski, S. B. Scott, R. Rao, K. Rigg, C. Zalities, J. Stevens, J. Sharman, G. Hinds and I. E. Stephens, *Johnson Matthey Technology Review*, 2024, **68**, 121-146.
9. N. T. T. Thao, J. U. Jang, A. K. Nayak and H. Han, *Small Science*, 2024, **4**, 2300109.
10. L. An, C. Wei, M. Lu, H. Liu, Y. Chen, G. G. Scherer, A. C. Fisher, P. Xi, Z. J. Xu and C. H. Yan, *Advanced materials*, 2021, **33**, 2006328.
11. S. W. Lee, C. Baik, D.-H. Kim and C. Pak, *Journal of Power Sources*, 2021, **493**, 229689.
12. Q. Wang, Y. Cheng, H. B. Tao, Y. Liu, X. Ma, D. S. Li, H. B. Yang and B. Liu, *Angewandte Chemie*, 2023, **135**, e202216645.
13. V. Pfeifer, T. E. Jones, J. J. Velasco Vélez, C. Massué, R. Arrigo, D. Teschner, F. Girgsdies, M. Scherzer, M. T. Greiner and J. Allan, *Surface and Interface Analysis*, 2016, **48**, 261-273.
14. R. V. Mom, L. J. Falling, O. Kasian, G. Algara-Siller, D. Teschner, R. H. Crabtree, A. Knop-Gericke, K. J. Mayrhofer, J.-J. s. Velasco-Vélez and T. E. Jones, *ACS Catalysis*, 2022, **12**, 5174-5184.
15. S. Geiger, O. Kasian, B. R. Shrestha, A. M. Mingers, K. J. Mayrhofer and S. Cherevko, *Journal of The Electrochemical Society*, 2016, **163**, F3132.
16. J. Xu, H. Jin, T. Lu, J. Li, Y. Liu, K. Davey, Y. Zheng and S.-Z. Qiao, *Science Advances*, 2023, **9**, eadh1718.
17. D. F. Abbott, D. Lebedev, K. Waltar, M. Povia, M. Nachtegaal, E. Fabbri, C. Copéret and T. J. Schmidt, *Chemistry of Materials*, 2016, **28**, 6591-6604.
18. C. Liang, R. R. Rao, K. L. Svane, J. H. Hadden, B. Moss, S. B. Scott, M. Sachs, J. Murawski, A. M. Frandsen and D. J. Riley, *Nature Catalysis*, 2024, 1-13.

19. S. Geiger, O. Kasian, M. Ledendecker, E. Pizzutilo, A. M. Mingers, W. T. Fu, O. Diaz-Morales, Z. Li, T. Oellers and L. Fruchter, *Nature Catalysis*, 2018, **1**, 508-515.
20. K. Schweinar, B. Gault, I. Mouton and O. Kasian, *The journal of physical chemistry letters*, 2020, **11**, 5008-5014.
21. O. Kasian, S. Geiger, T. Li, J.-P. Grote, K. Schweinar, S. Zhang, C. Scheu, D. Raabe, S. Cherevko and B. Gault, *Energy & Environmental Science*, 2019, **12**, 3548-3555.
22. M.-L. D. Tobias Binninger, *Energy & Environmental Science*, 2022/06/15, **15**.
23. S. Siracusano, V. Baglio, N. Van Dijk, L. Merlo and A. S. Aricò, *Applied energy*, 2017, **192**, 477-489.
24. S. A. Berlinger, X. Peng, X. Luo, P. J. Dudenas, G. Zeng, H. Yu, D. A. Cullen, A. Z. Weber, N. Danilovic and A. Kusoglu, *ACS Energy Letters*, 2024, **9**, 4792-4799.
25. D. Kulkarni, R. Ouimet, B. Erb, D. Y. Parkinson, H.-M. Chang, C. Wang, A. Smeltz, C. Capuano and I. V. Zenyuk, *ACS Applied Materials & Interfaces*, 2023, **15**, 48060-48071.
26. J. Knöppel, M. Möckl, D. Escalera-López, K. Stojanovski, M. Bierling, T. Böhm, S. Thiele, M. Rzepka and S. Cherevko, *Nature communications*, 2021, **12**, 2231.
27. T. Lazaridis, B. M. Stühmeier, H. A. Gasteiger and H. A. El-Sayed, *Nature Catalysis*, 2022, **5**, 363-373.
28. M. Bernt, A. Hartig-Weiß, M. F. Tovini, H. A. El-Sayed, C. Schramm, J. Schröter, C. Gebauer and H. A. Gasteiger, *Chemie Ingenieur Technik*, 2020/01/01, **92**.
29. M. Bernt, A. Siebel and H. A. Gasteiger, *Journal of The Electrochemical Society*, 2018, **165**, F305-F314.
30. M. Bernt, C. Schramm, J. Schröter, C. Gebauer, J. Byrknes, C. Eickes and H. Gasteiger, *Journal of The Electrochemical Society*, 2021, **168**, 084513.
31. A. P. D. Maja Milosevic, Mirjam Rogler, Andreas Hutzler, Thomas Böhm, Valentin Briega-Martos, Georgios Papakonstantinou, Michel Suermann, Simon Thiele, Kai Sundmacher, Serhiy Cherevko, 2025/10/06.
32. B. F. Selina Finger, Mingjian Wu, Leopold Lahn, Darius Hoffmeister, Johannes Will, Olga Kasian, Erdmann Spiecker, Simon Thiele, Anna T.S. Freiberg, Andreas Hutzler, *Energy & Environmental Science*, 2025/11/11, **18**.
33. D. Spernjak, R. Mukundan, R. L. Borup, L. G. Connolly, B. I. Zackin, V. D. Andrade, M. Wojcik, D. Y. Parkinson, D. L. Jacobson, D. S. Hussey, K. L. More, T. Chan, A. Z. Weber and I. V. Zenyuk, *ACS Applied Energy Materials*, September 28, 2018, **1**.
34. C. C. Weber, J. A. Wrubel, L. Gubler, G. Bender, S. De Angelis and F. N. Büchi, *ACS Applied Materials & Interfaces*, 2023, **15**, 34750-34763.
35. D. Kulkarni, A. Huynh, P. Satjaritanun, M. O'Brien, S. Shimpalee, D. Parkinson, P. Shevchenko, F. DeCarlo, N. Danilovic and K. E. Ayers, *Applied Catalysis B: Environmental*, 2022, **308**, 121213.
36. C. C. Weber, S. De Angelis, R. Meinert, C. Appel, M. Holler, M. Guizar-Sicairos, L. Gubler and F. N. Büchi, *EES Catalysis*, 2024, **2**, 585-602.
37. V. Pfeifer, T. Jones, J. V. Vélez, C. Massué, M. Greiner, R. Arrigo, D. Teschner, F. Girgsdies, M. Scherzer and J. Allan, *Physical Chemistry Chemical Physics*, 2016, **18**, 2292-2296.
38. N. a. Diklić, A. H. Clark, J. Herranz, D. Aegerter, J. S. Diercks, A. Beard, V. A. Saveleva, P. Chauhan, M. Nachtegaal and T. Huthwelker, *ACS Catalysis*, 2023, **13**, 11069-11079.
39. P. Liao, C. Chen, W. Ho, Y. Huang and K.-K. Tiong, *Thin Solid Films*, 1997, **301**, 7-11.
40. Z. Pavlovic, C. Ranjan, Q. Gao, M. van Gastel and R. Schlögl, *Acs Catalysis*, 2016, **6**, 8098-8105. DOI: 10.1039/D5TA08192K
41. F. Zhao, B. Wen, W. Niu, Z. Chen, C. Yan, A. Selloni, C. G. Tully, X. Yang and B. E. Koel, *Journal of the American Chemical Society*, 2021, **143**, 15616-15623.
42. C. Roiron, C. Wang, I. V. Zenyuk and P. Atanassov, *The Journal of Physical Chemistry Letters*, November 1, 2024, **15**.
43. R. Zhang, P. E. Pearce, V. Pimenta, J. Cabana, H. Li, D. Alves Dalla Corte, A. M. Abakumov, G. Rousse, D. Giaume and M. Deschamps, *Chemistry of Materials*, 2020, **32**, 3499-3509.
44. R.-S. Chen, Y.-S. Huang, Y.-M. Liang, D.-S. Tsai, Y. Chi and J.-J. Kai, *Journal of Materials chemistry*, 2003, **13**, 2525-2529.
45. F. Frati, M. O. Hunault and F. M. De Groot, *Chemical reviews*, 2020, **120**, 4056-4110.
46. K. J. Ferner, J. Park, Z. Kang, S. A. Mauger, M. Ulsh, G. Bender and S. Litster, *International Journal of Hydrogen Energy*, 2024, **59**, 176-186.
47. C. C. McCrory, S. Jung, J. C. Peters and T. F. Jaramillo, *Journal of the American Chemical Society*, 2013, **135**, 16977-16987.
48. M. Hüppauff and B. Lengeler, *Journal of the Electrochemical Society*, 1993, **140**, 598.
49. P. Steegstra, M. Busch, I. Panas and E. Ahlberg, *The Journal of Physical Chemistry C*, 2013, **117**, 20975-20981.
50. J. J. Velasco Vélez, D. Bernsmeier, R. V. Mom, P. Zeller, Y. Shao-Horn, B. Roldan Cuenya, A. Knop-Gericke, R. Schlögl and T. E. Jones, *Advanced Energy Materials*, 2024, **14**, 2303407.
51. C. Rozain, E. Mayousse, N. Guillet and P. Millet, *Applied Catalysis B: Environmental*, 2016, **182**, 153-160.
52. H. Gasteiger and S. Yan, *Journal of power sources*, 2004, **127**, 162-171.
53. R. Marić, C. Gebauer, F. Eweiner and P. Strasser, *Journal of The Electrochemical Society*, 2023, **170**, 084505.
54. S. M. Alia and G. C. Anderson, *Journal of The Electrochemical Society*, 2019, **166**, F282-F294.

View Article Online
DOI: 10.1039/D5TA08192K

Data availability statement

The data supporting this article have been included as part of the ESI.